Application of Machine Learning and Laser-Induced Breakdown Spectroscopy to Flame Spray Pyrolysis for the Prediction of Catalyst Properties

Can Wang, Ben Ko, Musa Najimu, and Erdem Sasmaz*

Read Online

ACCESS | 📊 Metrics & More | 📖 Article Recommendations | 🆘 Supporting Information

ABSTRACT: Flame spray pyrolysis (FSP) can rapidly synthesize nanomaterials with desired physical and chemical properties. However, the broad parameter space of FSP and postcharacterizations of the synthesized nanomaterials can slow down the material discovery process. In this work, we applied laser-induced breakdown spectroscopy (LIBS) and machine learning (ML) models to characterize catalysts' properties, which can decrease the number of postcharacterizations. The LIBS spectra are used as the descriptor to predict crystalline phase information, lattice constants (Å), and oxygen vacancy percentages (OV % s) of Ce−Mn−Zr solid solution catalysts by support vector classifiers and regressors. The balanced accuracies of making a correct prediction of phase information can reach 0.796, 0.829, 0.765, and 0.886 for tetragonal ZrO_2, tetragonal α-MnO_2, tetragonal β-MnO_2, and tetragonal Mn_3O_4 phases, respectively. The lattice constants and OV % s of the testing samples can be predicted with root-mean-squared errors of 0.04 and 0.05, respectively. These accuracies indicate that ML models can identify an inferred relation between emission spectra and catalysts' quality to determine the phase information, lattice constant (Å), and OV % of solid solution samples. Implementing LIBS and ML to FSP can provide rapid optimization of process parameters and rational guidance on novel material synthesis.
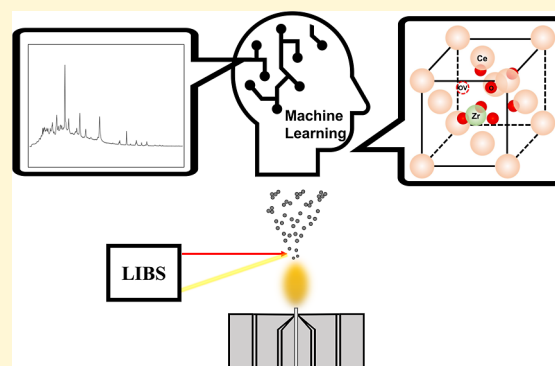
1. INTRODUCTION

Flame spray pyrolysis (FSP) provides a fast and continuous route for preparing nanosized catalysts in the range of 1−200 nm.[1] Nanoparticle synthesis through FSP allows for control over the production rate,[2,3] crystallite size,[4−6] crystalline phase,[7−9] oxygen vacancy percentage (OV %),[10,11] and material morphology,[12] which makes it an ideal technique for designing heterogeneous catalysts. However, optimizing the broad parameter space of FSP synthesis (e.g., liquid flow rate, oxygen flow rate, quenching rate, and pressure drop) and postsynthesis characterization of catalysts are often time-consuming, which retards the catalyst discovery. In situ characterizations such as laser-induced fluorescence (LIF), Raman spectroscopy, and UV−vis spectroscopy can be applied to FSP. LIF allows for good quantification of the species concentration in mixing processes[13,14] but does not reflect the chemical properties of nanoparticles formed in the synthesis. In situ Raman spectroscopy can probe the chemical composition,[15] but it may not be applied directly in the flame because the background signal of the flame cannot be separated well from the signal of interest. However, laser-induced breakdown spectroscopy (LIBS) can provide atomic spectral lines of elements[16−18] produced during FSP synthesis, which can be directly correlated with the catalyst morphology. Therefore, we implemented real-time LIBS to flame synthesis and adopted

the features in emission spectra into machine learning (ML) models to predict catalyst quality. Once ML models are generated, the description of catalyst quality can be obtained during the synthesis process, which can be an efficient approach to the rational synthesis of catalysts.

ML models, especially supervised learning algorithms, have been proven to be a valuable tool for establishing inferred relationships between the input (e.g., molecular parameters) and output (e.g., material physical properties and catalytic activity) without knowing the underlying principles. Many researchers used X-ray diffraction (XRD) patterns and selected atomic parameters as descriptors to predict lattice constants.[19−25] Dey et al. predicted the band gap energies of new chalcopyrites using chemical descriptors, including valency, atomic number, melting point, electronegativity, and pseudopotential radii available in the literature.[26] The predicted band gap energies were listed at different confidence levels and were found to be influenced mainly by the atomic

number and melting point. Recently, Li et al. investigated hydrogen production from wet organic wastes through supercritical water gasification. They used experimentally obtained data points such as feedstock composition, operational conditions, and catalytic descriptors, including transition metal properties, catalyst size, surface area, pore size, and pore volume of catalysts, collected from the literature. Their neural network model could predict syngas composition with an R^2 coefficient larger than 0.85.[27] In addition to the data set generated from experiments and literature, many publications on ML applications utilized data obtained by crystal field and charge transfer multiplet calculations to predict crystal-field parameters[28,29] or density functional theory to predict formation,[30] activation,[31] adsorption,[32,33] and binding energies[34] over transition metal surfaces. The large data set generated from theoretical calculations can provide detailed insight into the material properties but may not be adopted to predict oxygen vacancies and active sites accurately due to the complex metal−support interaction.

To date, only two studies have reported applications of ML in FSP synthesis. In one study, flame stability was detected in real time by analyzing the brightness of the anchor point of flame with ML, suggesting optimized process parameters for stable flame conditions.[35] Another study determined FSP parameters by combining ML and an in situ scanning mobility particle sizer to optimize the particle size distribution.[36] Considering the robustness of nanomaterial synthesis in FSP, there has not been any study that adopts guidance from emission spectroscopy in real time to identify catalysts' chemical properties and recommend FSP synthesis parameters. LIBS can be an ideal technique for monitoring and predicting catalyst quality during the FSP.[18,37,38] The features in the complex LIBS spectra can be trained using ML models to estimate the structural properties of the synthesized nanoparticles, such as crystalline phases, lattice constants, and OV % s, which are essential chemical properties that determine catalytic performance.[39,40]

In this work, a series of Pd/$Ce_xZr_yMn_z$ (where x, y, z = 0, 1, 2) solid solution catalysts were synthesized using FSP. The real-time LIBS was collected during nanoparticle formation and fed to the ML models to predict catalysts' chemical properties. Our results show that the ML models can recognize the LIBS patterns and relate them to catalysts' chemical parameters, limiting postcharacterization experiments.

2. EXPERIMENTS AND METHODS

2.1. Catalyst Synthesis. An FSP reactor was used to prepare Pd/$Ce_xZr_yMn_z$ (where x, y, z = 0, 1, 2) catalysts, as shown in Figure 1. Cerium (III) 2-ethylhexanoate (Alfa Aesar, 49% in 2-ethylhexanoic acid, 12% as Ce), zirconium(IV) oxide 2-ethylhexanoate (Alfa Aesar, in mineral spirits, ~6% as Zr), and manganese(II) 2-ethylhexanoate (Alfa Aesar, 40 % w/w in mineral spirits, 6% as Mn) were used as the precursors of Ce, Zr, and Mn, respectively. Palladium(II) acetylacetonate (Sigma-Aldrich, purity = 99%) was used as the precursor of Pd. The desired amounts of each precursor were dissolved in a 1:1 volumetric mixture of 2-ethylhexanolic acid (Sigma-Aldrich, purity ≥ 99%) and toluene (Sigma-Aldrich, anhydrous, purity = 99.8%). The molar ratios of elements Ce, Zr, and Mn were designed as 2:1:0, 1:1:0, 1:2:0, 2:0:1, 1:0:1, 1:0:2, 2:1:1, 1:1:1, and 1:2:1. The total molarity of precursors dissolved in fuel was 0.2, 0.3, and 0.4 M. The Pd content was fixed at 1 wt % in all samples. The precursor and fuel mixture solution was injected through the capillary of the stainless-steel gas-assisted atomizer (Schlick Atomizing technologies, Germany) by a syringe pump at a liquid feed rate of either 2 or 3 mL/ min (denoted as Lp, where p = 2, 3). Oxygen gas was delivered at flow
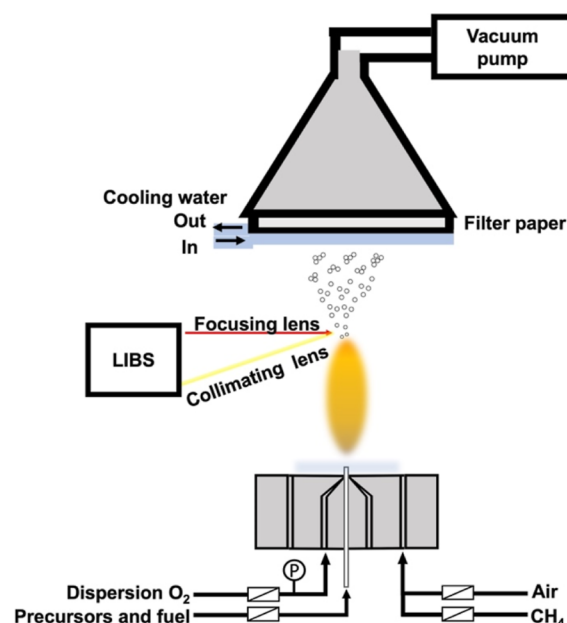

Figure 1. Experimental setup of FSP and in situ LIBS.

rates of either 4 or 5 L/min (denoted as Oq, where q = 4, 5) by a mass flow controller. The pressure drop at the nozzle tip was maintained at 1.5 bar. The injected liquid was dispersed by oxygen and ignited by the CH_4/air flat flame (CH_4: 1 L/min, air: 10 L/min). The formed nanoparticles were collected on a glass microfiber filter (Sigma-Aldrich, Grade GF/D, 257 mm in diameter) by a vacuum pump. Three reaction conditions were chosen for the experiments, that is, L2O5, L2O4, and L3O5. A total of 76 samples were synthesized. Due to the number of samples synthesized, a general nomenclature is used. The catalyst named 121-0.2-L2O5 was prepared with the element ratio of Ce/Zr/Mn = 1:2:1 and a total molarity of 0.2 M and synthesized at a liquid feed rate of 2 mL/min and an oxygen flow rate of 5 L/min.

2.2. Characterization of Catalysts. LIBS was carried out over a custom-built spectrometer designed by AccuStrata, Inc. A 1064 nm Q-switched Nd: YAG laser, operating with 100 A laser current, 10 ns pulse duration, and 10 Hz repetition rate, created the plasma. As shown in Figure 1, the laser was placed at a height of 70 mm above the burner, where the particles were already formed. Then, the plasma was formed by focusing the laser beam with a 4 in. focal length quartz lens. The light emitted from the plasma was collected by a collimating quartz lens coupled with a quartz fiber bundle. The fiber bundle transmitted photons to an imaging spectrometer (Ocean optics). The 200−900 nm spectral range was collected on the Catalyte Control Software (AccuStrata, Inc.).
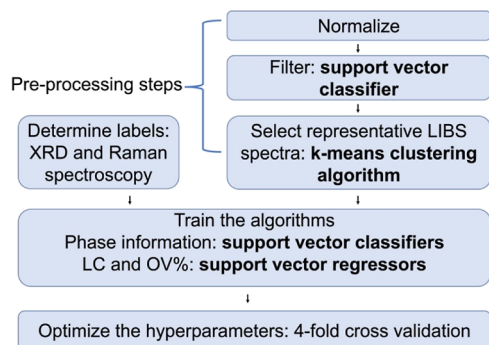
The as-synthesized samples were characterized on a LEXI-Rigaku Ultima III powder X-ray diffractometer, operated at 40 kV and 30 mA with a Cu Kα source (λ = 0.154 nm). The 2θ values ranging from 20 to 80° were collected with a 0.02° step size and a scanning rate of 2°/ min. Background correction and Kα_2 stripping were accomplished using the Rigaku data analysis software. The lattice constants for the as-synthesized samples were calculated by Bragg's law. Raman spectra were acquired over a customized optical microscopy platform based on the Renishaw inVia Raman microscope with a 532 nm (1.1 mW) excitation source. Raman spectra were collected in a frequency range of 200−800 cm^{-1}. Oxygen vacancies of the samples were calculated using the peak area of δ, and F_{2g} bands were calculated using eq 1

$$OV \% = \frac{A_\delta}{A_{F_{2g}} + A_\delta} \times 100\%$$

(1)

where A_δ and $A_{F_{2g}}$ are areas of δ and F_{2g} bands, respectively.

2.3. ML Methodology. The data preprocessing and ML methodology used in this work are summarized in Scheme 1.

Scheme 1. Flow Diagram of the Developed ML Process to Achieve a Prediction of Catalyst Quality

Pre-processing steps —
- Normalize
- Filter: **support vector classifier**
- Determine labels: XRD and Raman spectroscopy
- Select representative LIBS spectra: **k-means clustering algorithm**

Train the algorithms
Phase information: **support vector classifiers**
LC and OV%: **support vector regressors**

Optimize the hyperparameters: 4-fold cross validation

For both the training and predicting processes, three preprocessing procedures are used: (1) normalization, (2) filtration, and (3) selection of representative LIBS spectra. The raw LIBS spectra were loaded into the algorithm and were normalized by eq 2

$$I_{j,\text{-norm}} = \frac{I_j - I_{\min}}{I_{\max} - I_{\min}} \tag{2}$$

where I_j is the jth intensity value of one raw spectrum, $I_{\min}$ is the minimum intensity value of that raw spectrum, $I_{\max}$ is the maximum intensity value of that raw spectrum, and $I_{j,\text{int-norm}}$ is the normalized jth intensity value of the spectrum. After normalization, the spectra were fed to a filtering support vector classifier (SVCs) (kernel function: linear, penalty factor C value = 4) to filter out spectra with no particle information. Distinct peaks could be observed if the laser successfully hit the particles and generated plasma, as shown in Figure 2a. A spectrum showed no distinguishable peak characteristics (Figure 2b) and significant noise variations if the flame overwhelmed the LIBS signal or the laser missed the particles (Figure 2c), respectively. These "missed" and "overwhelmed" spectra were filtered out, and no further data processing was performed.

An unsupervised k-means clustering algorithm was performed on all of the "hit" spectra of the sample and split into 10 clusters. The details of determining an optimized number of clusters are introduced in the Supporting Information and Figure S1. The spectrum closest to the centroid of each cluster was selected as the representative spectrum for that cluster; therefore, 10 representative spectra were chosen to represent that sample. This "clustering and selecting" process was required to eliminate data redundancy, decrease the training time, recognize the commonalities, and increase the tolerance of any variance. After clustering, 2048 intensities at each wavelength in the representative LIBS spectra were used as the input information in training and predicting processes.

After the data preprocessing, among the total of 76 samples, 68 samples were randomly selected as training and validation samples to optimize hyperparameters for each model. Four-fold cross-validation was for hyperparameter determination; hence, there were 17 validation and 51 training samples in each fold. If one sample was used as the validation dataset in one of the fourfold, then that sample was not used as a validation dataset in other folds. Samples 1−17, 18−34, 35−51, and 52−68 were used as the validation dataset in cross-validation folds 4, 3, 2, and 1, respectively. The results from the optimization procedure are shown in Tables S1−S4, S6, and S8. The hyperparameters are summarized in Tables S5, S7, and S9. The averaged hyperparameters were used in the optimized models. The remaining eight samples (no. 69−76) were used as the testing samples, which did not participate in the optimized model determination process, to determine whether the optimized models can predict chemical properties.
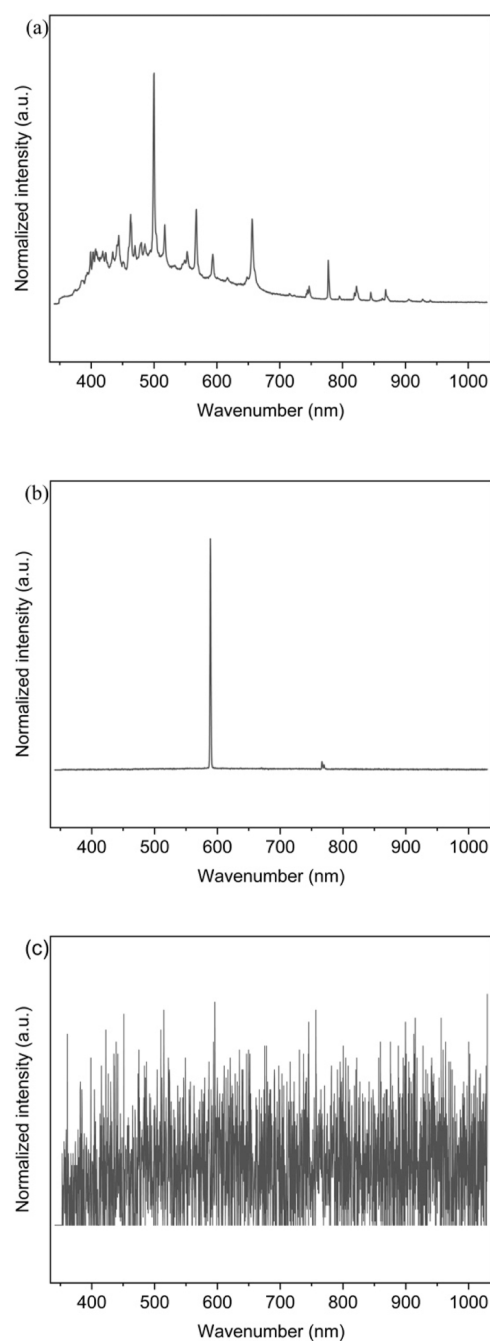
Figure 2. Examples of the LIBS spectrum. (a) The laser "hit" the particles, plasma was generated, and a LIBS signal was collected. (b) The laser went through the flame, and the flame peak "overwhelmed" the LIBS signal of particles. (c) The laser "missed" the particle, and no LIBS signal was collected.

In the training process, experimentally determined phase information, lattice constants, and OV % s were used to label the representative LIBS spectra. For each sample, 10 representative LIBS spectra were fed into models to predict the chemical properties of the sample. Four optimized SVCs and two optimized support vector regressors (SVRs) were applied. SVC and regressor modules were imported from the Scikit-learn ML Python library. The SVCs were used in predicting the presence or absence of the tetragonal ZrO_2 phase (kernel function: RBF, penalty factor C value = 4), tetragonal α-MnO_2 phase (kernel function: RBF, penalty factor C value = 4), tetragonal β-MnO_2 phase (kernel function: RBF, penalty factor C value = 3.5), and tetragonal Mn_3O_4 phase (kernel function: RBF,

penalty factor C value = 3.5). The probability of making a correct prediction for each sample was provided. For example, a probability of 80% meant that there were 8 out of 10 predicted results, in accord with the experimentally determined phase information. Besides, recall, precision, and F1 score were also calculated using eqs 3−5 to evaluate the performance of SVCs in predicting phase information. The SVRs were used to predict the lattice constants (kernel function: RBF, penalty factor C value = 100, maximum error $\epsilon = 5.25 \times 10^{-7}$) and OV % s (kernel function: RBF, penalty factor C value = 100, maximum error $\epsilon = 1 \times 10^{-6}$). For SVR models, the average of 10 predicted values was used as the final predicted value of that sample. The coefficient of determination (R^2), root mean squared error (RMSE), and mean average error (MAE) were calculated using eqs 6−8

$$Recall = \frac{true\ positive}{true\ positive\ +\ false\ negative} \quad (3)$$

$$Precision = \frac{true\ positive}{true\ positive\ +\ false\ positive} \quad (4)$$

$$F1\ score = \frac{2 \times precision \times recall}{precision\ +\ recall} \quad (5)$$

$$R^2 = 1 - \frac{\sum_{i=1}^{N} (y_i - \hat{y}_i)^2}{\sum_{i=1}^{N} (y_i - \bar{y})^2} \quad (6)$$

$$RMSE = \sqrt{\frac{\sum_{i=1}^{N} (y_i - \hat{y}_i)^2}{N}} \quad (7)$$

$$MAE = \frac{\sum_{i=1}^{N} |y_i - \hat{y}_i|}{N} \quad (8)$$

where N is the number of data points, y is the experimentally determined value, $\hat{y}$ is the predicted result, and $\bar{y}$ is the average of the experimentally determined values of N samples.

3. RESULTS

3.1. Sample Characterization and Label Assignment.
The crystalline structure of the as-synthesized Ce−Zr, Ce−Mn, and Ce−Zr−Mn sample groups was determined using XRD and Raman spectroscopy. As shown in Figure 3, the samples can be classified as single- or multiphase structures affected by the synthesis conditions and molar ratios of metal precursors. The diffraction patterns of the 201-0.2-L2O5 and 210-0.2-L2O5 samples in Figure 3a are examples of the single-phase samples attributed to the cubic fluorite structure.[41,42] No additional diffraction peaks are observed, indicating that these samples are composed of a single phase, where Ce_2Mn_1 and Ce_2Zr_1 solid solutions are formed. The XRD patterns of the multiphase structures are shown as an example in Figure 3b. The diffraction peaks marked with red, green, blue, and purple indices are assigned to the tetragonal phases of ZrO_2,[43] Mn_3O_4,[44] α-MnO_2 (JCPDS no.44−0141),[45] and β-MnO_2 (JPCDS no.24−0735),[46,47] respectively. It is important to note that diffraction peaks of Pd species cannot be observed due to their low amount and high dispersion. Analysis of all samples with XRD showed similar phases and presented up to five crystal structures: cubic CeO_2 and tetragonal phases of ZrO_2, Mn_3O_4, α-MnO_2, and β-MnO_2. The lattice constant of each sample ranges between 5.19 and 5.41 Å depending on the composition and formation of the solid solution, as shown in Table S10. The phase presence or absence and lattice constant of each sample were used as a label in the supervised ML
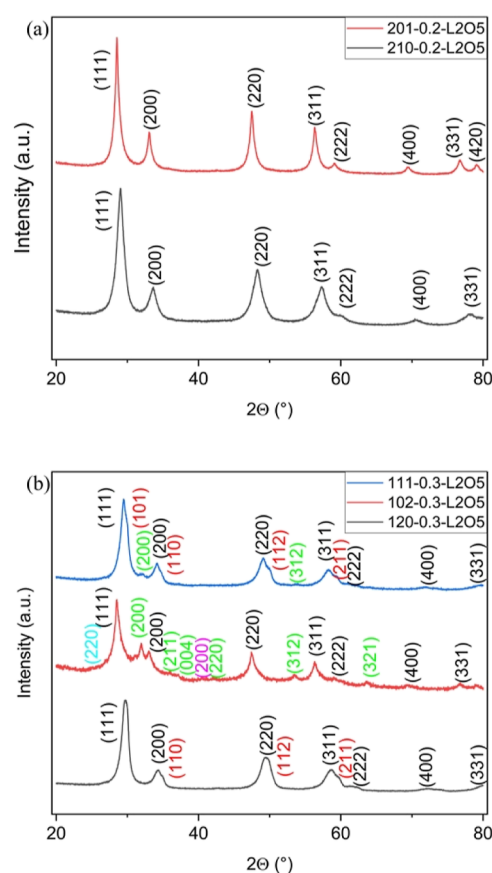

Figure 3. (a) Powder XRD pattern for the (a) 201-0.2-L2O5 and 210-0.2-L2O5 samples and (b) 111-0.3-L2O5, 102-0.3-L2O5, and 120-0.3-L2O5 samples.

model. For multiphase samples, the lattice constant of the dominant cubic structure is used.

The Raman spectra can provide information, including oxygen lattice vibrations, crystal symmetry, and types of defects in the crystal structure of the samples. The Raman spectra can also confirm the formation of a single phase, as shown in Figure 4. The vibrational band located at 450−460 cm^{-1} can be assigned to the F_{2g} band due to the symmetric breathing mode of the O atoms around Ce ions in the fluorite structure.[48−52] No other phases can be observed in the
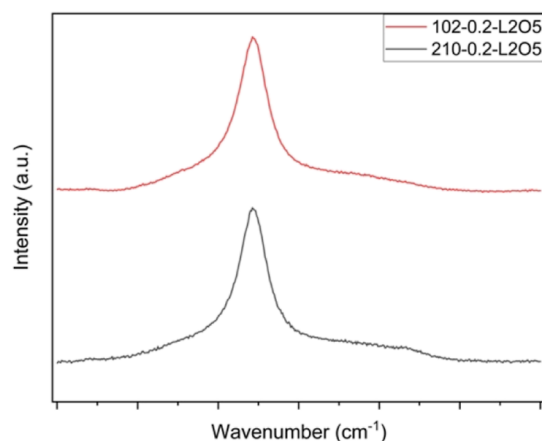

Figure 4. Raman spectra for the 201-0.2-L2O5 and 210-0.2-L2O5 samples.

Raman spectra, consistent with the XRD analysis. Only three representative spectra for the Ce−Zr, Ce−Mn, and Ce−Zr−Mn sample groups were chosen to discuss the band assignments as the peak assignments of these representative examples are similar among their own sample groups. The 120-0.2-L2O5 sample is selected as an example for the Ce−Zr sample group. Five main bands located at 255 (α), 305 (β), 457 (F_{2g}), 560 (δ), and 630 (γ) cm^{-1} are observed in the spectra, as shown in Figure 5a. The band at 457 cm^{-1} belongs to the F_{2g} symmetry of the fluorite structure. Compared to the F_{2g} band of pure CeO$_2$,[53] the F_{2g} band of the 120-0.2-L2O5 sample shifts to a lower wavenumber, indicating a weaker bonding between the metal and oxygen atoms due to the partial substitution of Ce^{4+} by Zr^{4+} cations and distortion in the lattice. In addition, the broadening of the F_{2g} peak may be associated with incorporating Zr^{4+} cations into the CeO$_2$ lattice.[48] The bands observed above 500 cm^{-1} can be split into two peaks, centered on 560 (δ) and 630 (γ) cm^{-1}, respectively. The δ band is assigned to defect structures, including an O^{2-} ion vacancy in the CeO$_2$ lattice,[39,48] whereas the γ band is induced by the ZrO$_8$-type defect.[39,54,55] For the bands below 350 cm^{-1}, the α band is attributed to the t-phase of ZrO$_2$,[48] while the β band belongs to the t″-phase of ZrO$_2$.[39] The 102-0.3-L2O5 sample is chosen to discuss the Raman peak assignments for the Ce−Mn sample group. Four main bands located at 360 (σ), 447 (F_{2g}), 540 (δ), and 635 (ω) cm^{-1} are observed, as shown in Figure 5b. The vibrational band's σ and ω are formed after the incorporation of Mn, where the σ band corresponds to the Mn−O−Mn stretching mode of MnO$_x$ or Mn$_3$O$_4$ species.[56−58] The ω band is induced by the A$_{1g}$ mode of MnO$_x$ or Mn$_3$O$_4$ species due to the Mn−O breathing vibration of divalent Mn ions in tetrahedral coordination.[56,59−62] The Raman spectra of the FSP-made 1 wt % Pd/MnO$_x$ sample can validate the peak assignments of the σ and ω bands, as shown in the inset of Figure 5b. The wavenumbers of the σ and ω bands of Pd/MnO$_x$ match the Ce−Mn sample group well. The Raman spectrum of the sample 111-0.4-L2O4 is shown in Figure 5c as a representative example for the Ce−Zr−Mn sample group. Six vibration bands at 255 (α), 309 (β), 370 (σ), 463 (F_{2g}), 550 (δ), and 620 (ϕ) cm^{-1} are observed. The band assignments are similar to the discussion above. It is possible that the additional ϕ band could be due to the ZrO$_8$-type defect or the Mn−O−Mn stretching mode of Mn$_3$O$_4$.

3.2. Prediction of Phase Presence, Lattice Constants, and Oxygen Vacancy Percentages.
The optimized SVC models were used to predict phase presence or absence using the representative LIBS spectra of each sample. The confusion matrixes are provided in Supporting Information Tables S11−S18. The evaluations for SVC models on predicting phase information over all samples and testing samples are shown in Table 1. The prediction of the cubic CeO$_2$ phase is excluded here as all samples have a fluorite crystal structure. Among our 76 samples, up to eight samples showed α-MnO$_2$ and/or β-MnO$_2$ phases. Because the testing samples are chosen randomly, samples may not show α-MnO$_2$ and β-MnO$_2$ phases. Sensitivity and specificity are calculated due to the imbalanced data feature. The balanced accuracies of predicting the tetragonal ZrO$_2$, α-MnO$_2$, β-MnO$_2$, and Mn$_3$O$_4$ phases for the 76 samples are 0.796, 0.829, 0.765, and 0.886, respectively. When phases are predicted for the eight testing samples, the balanced accuracies predicting the tetragonal ZrO$_2$ and Mn$_3$O$_4$ phases decrease to 0.625 and 0.806, respectively. The low
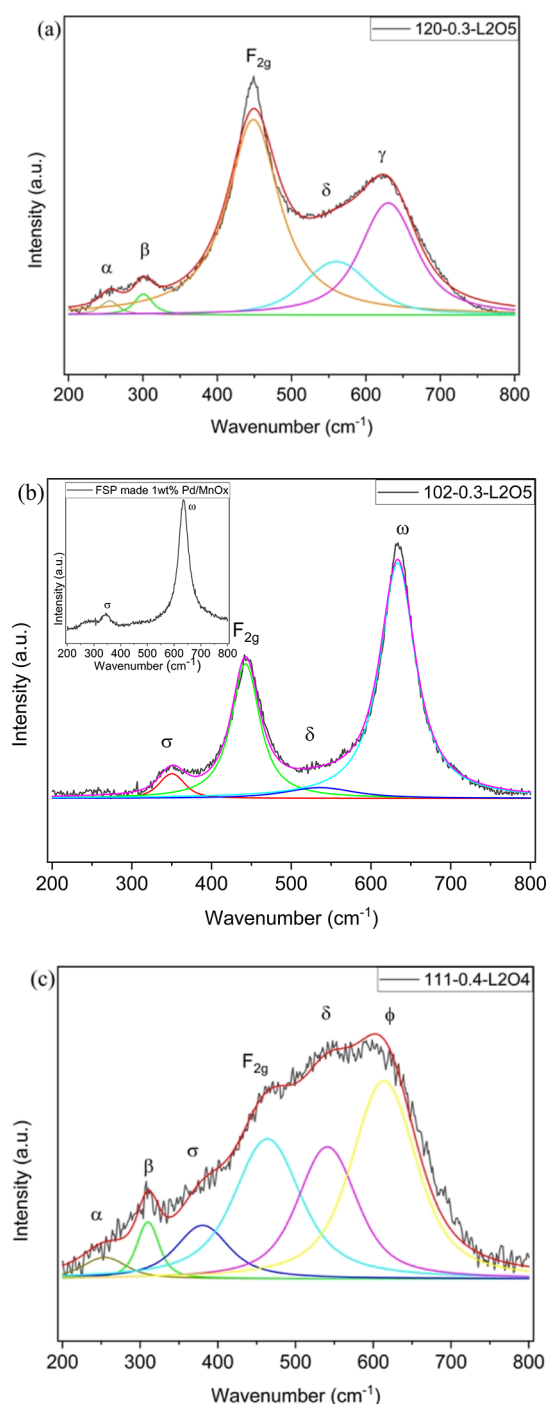

Figure 5. Raman spectra for the (a) 120-0.2-L2O5, (b) 102-0.3-L2O5, and (c) 111-0.4-L2O4 samples. Peaks α and β belong to the t-phase and t″-phase of ZrO$_2$, respectively. The F_{2g} peak is the symmetric breathing mode of the Ce−O bond. Peaks δ and γ represent the defect structure of oxygen vacancy and the ZrO$_8$-type defect, respectively. Peaks σ and ω correspond to the stretching mode and breathing vibration of MnO$_x$ or Mn$_3$O$_4$ species, respectively.

balanced accuracy for predicting the tetragonal ZrO$_2$ phase in testing samples might be due to the complex crystalline structure of the Ce$_x$Zr$_{1−x}$O$_2$ solid solution. The metastable t″- or t′-phases[39,63] can exist during the high-temperature related cubic−tetragonal phase transition in the Ce$_x$Zr$_{1−x}$O$_2$ solid solution, where oxygen displacement can be observed. The t″-phase has been detected as the β band in Figure 5a, while the γ

Table 1. Evaluations for Predictions of Phase Information over All Samples and Testing Samples[a]

	ZrO_2	α-MnO_2	β-MnO_2	Mn_3O_4
	All Samples			
recall	0.647	0.667	0.533	0.911
precision	0.921	0.769	0.842	0.848
F1 score	0.760	0.714	0.653	0.878
accuracy	79.6%	97.9%	97.8%	88.4%
sensitivity	0.647	0.667	0.533	0.911
specificity	0.945	0.991	0.996	0.861
balanced accuracy	0.796	0.829	0.765	0.886
	Testing Samples			
recall	0.400	N/A	N/A	0.833
precision	0.727	0	0	0.694
F1 score	0.516	N/A	N/A	0.757
accuracy	62.5%	92.5%	96.3%	80.0%
sensitivity	0.400	N/A	N/A	0.833
specificity	0.850	0.925	0.963	0.780
balanced accuracy	0.625	N/A	N/A	0.806

[a]The prediction results were determined by the RBF models with optimized hyperparameter C-values of 4, 4, 3.5, and 3.5 for ZrO_2, α-MnO_2, β-MnO_2, and Mn_3O_4 phases, respectively.

band could overlap the t'-phase peak in Figure 5a. This complex structure of samples can make it challenging to recognize and relate the phase information to the LIBS pattern. The performance of SVC in predicting the Mn_3O_4 phase is pretty good.

The lattice constants predicted by the SVR model for all samples are shown in Table 2 and compared with measured
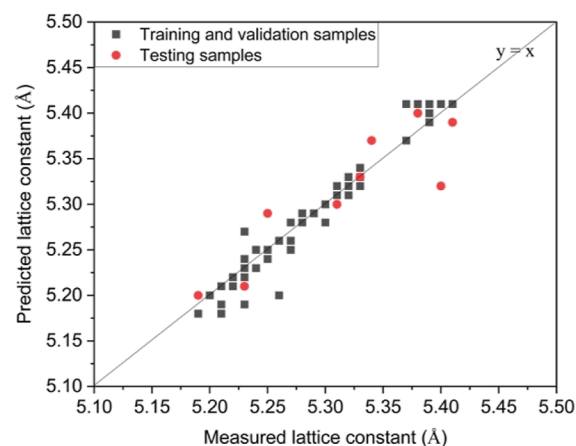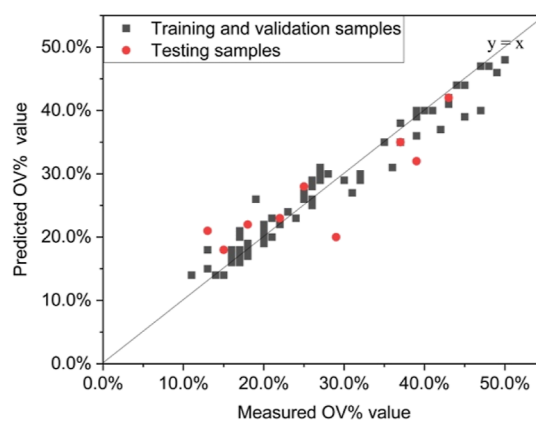
Table 2. Measured and Predicted Lattice Constant and Oxygen Vacancy Percentage of All Samples[a]

	lattice constant (Å)	oxygen vacancy percentage
MAE for 8 testing samples	0.03	0.05
R^2 for 8 testing samples	0.78	0.76
RMSE for 8 testing samples	0.04	0.05
MAE for all 76 samples	0.01	0.02
R^2 for all 76 samples	0.94	0.94
RMSE for all 76 samples	0.02	0.03

[a]The prediction results were determined by the RBF models with an optimized hyperparameter C value of 100 and an ε-value of 5.25×10^{-7} for lattice constants and a C value of 12.5 and an ε-value of 1×10^{-6} for OV % s.

lattice constants in Figure 6. The predicted and measured lattice constants have an excellent alignment with an R^2 coefficient of 0.94 among all 76 samples. The RMSE, MAE, and R^2 coefficients for eight testing samples are calculated to be 0.04, 0.03, and 0.74, respectively. The calculated OV % s from Raman spectroscopy and predicted OV % s from the SVR model are shown in Table 1 and Figure 7. The SVR model can predict the OV % for all samples with the RMSE, MAE, and R^2 coefficients of 0.03, 0.02, and 0.94, respectively. Again, applying the SVR model for the testing samples increases the RMSE and MAE to 0.05 and decreases the R^2 coefficient to 0.76.

The RMSE and MAE for predicting the lattice constants are slightly higher than the training and validation datasets. Considering the complexity of LIBS spectra, the accuracy of the lattice constant prediction is comparable to the literature.

Figure 6. Comparison between measured and predicted lattice constants (black square represents the training and validation datasets; red circle represents the testing dataset).

Figure 7. Comparison between measured and predicted OV % s (black square represents the training and validation datasets; red circle represents the testing dataset).

Several works have reported the prediction of lattice constants of metal oxides, perovskites, and alloys using ML models.[19−24] A wide range of data set sizes ranging from 82 to 18,000 samples were applied to train the ML models to predict lattice constants with well-defined atomic parameters (e.g., atomic radii, bond length, and angles between cell edges). Zhang et al. developed four ML models to predict the lattice constant of 167 spinel compounds and showed that the mean RMSE and MAE could range between 0.04 and 0.17 and 0.02 and 0.13, respectively.[22] Compared with the literature, the SVR model can successfully predict the lattice constants of solid solutions.

Overall, SVC and SVR models are shown to be a powerful data-driven approach for finding patterns and trends among high-dimensional data. Considering the dataset size, the SVC and SVR models can reasonably predict the phase presence, lattice constants, and OV % s of $Pd/Ce_xZr_yMn_z$ nanomaterials. The error generated by ML models can be ascribed to the complexities intrinsic to LIBS spectra. The ML models must capture any change in LIBS patterns generated by the 2048 feature and relate them to the catalyst quality. The complexities of LIBS spectra certainly increase the difficulty in the training process. It is important to note that the accuracy of the ML models can also depend on experimental uncertainties such as pressure drop at the nozzle tip and fluctuations in flame height. The changes in pressure drop can affect the precursor

liquid dispersion, which might affect particle growth speed. The laser at a fixed height above the burner can contact solid-phase particles at different formation stages (e.g., primary particles and agglomerated particles), influencing the LIBS spectra. However, the *k*-means clustering algorithm was utilized to diminish the error/uncertainty caused by the synthesis. For one sample, no matter how many LIBS spectra were collected, their LIBS pattern should be ideally the same. The *k*-means clustering algorithm (Table S1) suggested that there were 10 representative LIBS patterns for one sample; the difference among these 10 patterns should be due to the error/uncertainty of the experiments. We have trained the models to correlate that sample's chemical properties with these 10 patterns so that the models themselves have the ability to relate the chemical properties to the LIBS spectra collected under specific synthesis conditions.

4. CONCLUSIONS

The real-time LIBS and ML models were applied to predict the chemical properties of the nanoparticles synthesized by FSP. The SVC and SVR models predict phase presence, lattice constant, and OV % s of the Ce−Zr−Mn-based catalysts. Our results show that the average accuracy of predicting phase formation can reach 0.82. Both the lattice constant and OV % s of $Pd/Ce_xZr_yMn_z$ can be predicted well, with R^2 coefficients of testing samples reaching up to 0.76. Despite the complexity of the LIBS patterns, the SVC and SVR models have shown good performances.

FSP is a fast and controllable synthesis technique for the rational synthesis of nanomaterials. This work shows that ML models can improve the efficiency of nanoparticle synthesis in FSP. The ML models can optimize FSP process parameters to synthesize solid solution catalysts with desired phases, lattice constants, and OV % s. Additionally, the developed ML models open possibilities to characterize catalysts' quality using real-time LIBS rapidly and can eliminate catalysts' postsynthesis characterization.

■ ASSOCIATED CONTENT

ⓢ Supporting Information

The Supporting Information is available free of charge at https://pubs.acs.org/doi/10.1021/acs.chemmater.2c03119.

Determination of the optimum cluster number among LIBS spectra; detailed hyperparameter tuning process; predicted results in validation datasets by the models trained by corresponding training datasets; and optimized hyperparameters obtained after the cross-validation process (PDF)

■ AUTHOR INFORMATION

Corresponding Author

Erdem Sasmaz − *Department of Chemical and Biomolecular Engineering, University of California, Irvine, California 92697, United States;* ⓞ orcid.org/0000-0002-4861-9406; Email: esasmaz@uci.edu

Authors

Can Wang − *Department of Chemical and Biomolecular Engineering, University of California, Irvine, California 92697, United States*

Ben Ko − *Department of Chemical and Biomolecular Engineering, University of California, Irvine, California 92697, United States*

Musa Najimu − *Department of Chemical and Biomolecular Engineering, University of California, Irvine, California 92697, United States*

Complete contact information is available at:
https://pubs.acs.org/10.1021/acs.chemmater.2c03119

■ REFERENCES

(1) Teoh, W. Y.; Amal, R.; Mädler, L. Flame Spray Pyrolysis: An Enabling Technology for Nanoparticles Design and Fabrication. *Nanoscale* **2010**, *2*, 1324−1347.

(2) Mädler, L.; Kammler, H. K.; Mueller, R.; Pratsinis, S. E. Controlled Synthesis of Nanostructured Particles by Flame Spray Pyrolysis. *J. Aerosol Sci.* **2002**, *33*, 369−389.

(3) Mueller, R.; Mädler, L.; Pratsinis, S. E. Nanoparticle Synthesis at High Production Rates by Flame Spray Pyrolysis. *Chem. Eng. Sci.* **2003**, *58*, 1969−1976.

(4) Mueller, R.; Jossen, R.; Kammler, H. K.; Pratsinis, S. E.; Akhtar, M. K. Growth of Zirconia Particles Made by Flame Spray Pyrolysis. *AIChE J.* **2004**, *50*, 3085−3094.

(5) Torabmostaedi, H.; Zhang, T.; Foot, P.; Dembele, S.; Fernandez, C. Process Control for the Synthesis of ZrO_2 Nanoparticles Using FSP at High Production Rate. *Powder Technol.* **2013**, *246*, 419−433.

(6) Noriler, D.; Rosebrock, C. D.; Madler, L.; Meier, H. F.; Fritsching, U. Influence of Atomization and Spray Parameters on the Flame Spray Process for Nanoparticle Production. *Atomization Sprays* **2014**, *24*, 495−524.

(7) Tok, A. I. Y.; Boey, F. Y. C.; Zhao, X. L. Novel Synthesis of Al_2O_3 Nano-Particles by Flame Spray Pyrolysis. *J. Mater. Process. Technol.* **2006**, *178*, 270−273.

(8) Laine, R. M.; Marchal, J.; Sun, H.; Pan, X. Q. A New $Y_3Al_5O_{12}$ Phase Produced by Liquid-Feed Flame Spray Pyrolysis (LF-FSP). *Adv. Mater.* **2005**, *17*, 830−833.

(9) Baker, C.; Kim, W.; Sanghera, J.; Goswami, R.; Villalobos, G.; Sadowski, B.; Aggarwal, I. Flame Spray Synthesis of Lu_2O_3 Nanoparticles. *Mater. Lett.* **2012**, *66*, 132−134.

(10) Zhang, Z.; Yu, J.; Zhang, J.; Ge, Q.; Xu, H.; Dallmann, F.; Dittmeyer, R.; Sun, J. Tailored Metastable Ce-Zr Oxides with Highly Distorted Lattice Oxygen for Accelerating Redox Cycles. *Chem. Sci.* **2018**, *9*, 3386−3394.

(11) Gunawan, C.; Lord, M. S.; Lovell, E.; Wong, R. J.; Jung, M. S.; Oscar, D.; Mann, R.; Amal, R. Oxygen-Vacancy Engineering of Cerium-Oxide Nanoparticles for Antioxidant Activity. *ACS Omega* **2019**, *4*, 9473−9479.

(12) Kim, M.; Laine, R. M. One-Step Synthesis of Core-Shell $(Ce_{0.7}Zr_{0.3}O_2)_x (Al_2O_3)_{1-x} [(Ce_{0.7}Zr_{0.3}O_2)@ Al_2O_3]$ Nanopowders via Liquid-Feed Flame Spray Pyrolysis (LF-FSP). *J. Am. Chem. Soc.* **2009**, *131*, 9220−9229.

(13) Rüttinger, S.; Spille, C.; Hoffmann, M.; Schlüter, M. Laser-Induced Fluorescence in Multiphase Systems. *ChemBioEng Rev.* **2018**, *5*, 253−269.

(14) Mannazhi, M.; Bergqvist, S.; Bengtsson, P.-E. Influence of Potassium Chloride on PAH Concentration during Soot Formation Studied Using Laser-Induced Fluorescence. *Combust. Flame* **2022**, *235*, 111709.

(15) Bentrup, U. Combining in Situ Characterization Methods in One Set-up: Looking with More Eyes into the Intricate Chemistry of the Synthesis and Working of Heterogeneous Catalysts. *Chem. Soc. Rev.* **2010**, *39*, 4718.

(16) Harmon, R. S.; Senesi, G. S. Laser-Induced Breakdown Spectroscopy - A geochemical tool for the 21st century. *Appl. Geochem.* **2021**, *128*, 104929.

(17) Stavropoulos, P.; Michalakou, A.; Skevis, G.; Couris, S. Quantitative Local Equivalence Ratio Determination in Laminar Premixed Methane-Air Flames by Laser Induced Breakdown Spectroscopy (LIBS). *Chem. Phys. Lett.* **2005**, *404*, 309−314.

(18) Ren, Y.; Ran, K.; Kruse, S.; Mayer, J.; Pitsch, H. Flame Synthesis of Carbon Metal-Oxide Nanocomposites in a Counterflow Burner. *Proc. Combust. Inst.* **2021**, *38*, 1269−1277.

(19) Majid, A.; Khan, A.; Javed, G.; Mirza, A. M. Lattice Constant Prediction of Cubic and Monoclinic Perovskites Using Neural Networks and Support Vector Regression. *Comput. Mater. Sci.* **2010**, *50*, 363−372.

(20) Zhang, Y.; Xu, X. Machine Learning Lattice Parameters of Monoclinic Double Perovskites. *Int. J. Quantum Chem.* **2020**, *121*, No. e26480.

(21) Zhang, Y.; Xu, X. Machine Learning Modeling of Lattice Constants for Half-Heusler Alloys. *AIP Adv.* **2020**, *10*, 045121.

(22) Zhang, Y.; Xu, X. Machine Learning Lattice Constants for Spinel Compounds. *Chem. Phys. Lett.* **2020**, *760*, 137993.

(23) Li, Y.; Yang, W.; Dong, R.; Hu, J. Mlatticeabc: Generic Lattice Constant Prediction of Crystal Materials Using Machine Learning. *ACS Omega* **2021**, *6*, 11585−11594.

(24) Javed, S. G.; Khan, A.; Majid, A.; Mirza, A. M.; Bashir, J. Lattice Constant Prediction of Orthorhombic ABO3 Perovskites Using Support Vector Machines. *Comput. Mater. Sci.* **2007**, *39*, 627−634.

(25) Takahashi, K.; Takahashi, L.; Baran, J. D.; Tanaka, Y. Descriptors for Predicting the Lattice Constant of Body Centered Cubic Crystal. *Chem. Phys.* **2017**, *146*, 204104.

(26) Dey, P.; Bible, J.; Datta, S.; Broderick, S.; Jasinski, J.; Sunkara, M.; Menon, M.; Rajan, K. Informatics-Aided Bandgap Engineering for Solar Materials. *Comput. Mater. Sci.* **2014**, *83*, 185−195.

(27) Li, J.; Pan, L.; Suvarna, M.; Wang, X. Machine Learning Aided Supercritical Water Gasification for H2-Rich Syngas Production with Process Optimization and Catalyst Screening. *J. Chem. Eng.* **2021**, *426*, 131285.

(28) Zheng, C.; Mathew, K.; Chen, C.; Chen, Y.; Tang, H.; Dozier, A.; Kas, J. J.; Vila, F. D.; Rehr, J. J.; Piper, L. F. J.; Persson, K. A.; Ong, S. P. Automated Generation and Ensemble-Learned Matching of X-Ray Absorption Spectra. *NPJ Comput. Mater.* **2018**, *4*, 12.

(29) Suzuki, Y.; Hino, H.; Kotsugi, M.; Ono, K. Automated Estimation of Materials Parameter from X-Ray Absorption and Electron Energy-Loss Spectra with Similarity Measures. *NPJ Comput. Mater.* **2019**, *5*, 39.

(30) García-Muelas, R.; López, N. Statistical Learning Goes beyond the D-Band Model Providing the Thermochemistry of Adsorbates on Transition Metals. *Nat. Commun.* **2019**, *10*, 4687.

(31) Artrith, N.; Lin, Z.; Chen, J. G. Predicting the Activity and Selectivity of Bimetallic Metal Catalysts for Ethanol Reforming Using Machine Learning. *ACS Catal.* **2020**, *10*, 9438−9444.

(32) Li, Z.; Ma, X.; Xin, H. Feature Engineering of Machine-Learning Chemisorption Models for Catalyst Design. *Catal. Today* **2017**, *280*, 232−238.

(33) Li, Z.; Wang, S.; Chin, W. S.; Achenie, L. E.; Xin, H. High-Throughput Screening of Bimetallic Catalysts Enabled by Machine Learning. *J. Mater. Chem. A* **2017**, *5*, 24131−24138.

(34) Gu, G. H.; Noh, J.; Kim, S.; Back, S.; Ulissi, Z.; Jung, Y. Practical Deep-Learning Representation for Fast Heterogeneous Catalyst Screening. *J. Phys. Chem. Lett.* **2020**, *11*, 3185−3191.

(35) Pan, J.; Libera, J. A.; Paulson, N. H.; Stan, M. Flame Stability Analysis of Flame Spray Pyrolysis by Artificial Intelligence. *Int. J. Adv. Des. Manuf.* **2021**, *114*, 2215−2228.

(36) Paulson, N. H.; Libera, J. A.; Stan, M. Flame spray pyrolysis optimization via statistics and machine learning. *Mater. Des.* **2020**, *196*, 108972.

(37) Zhang, Y.; Xiong, G.; Li, S.; Dong, Z.; Buckley, S. G.; Tse, S. D. Novel Low-Intensity Phase-Selective Laser-Induced Breakdown Spectroscopy of TiO2 Nanoparticle Aerosols during Flame Synthesis. *Combust. Flame* **2013**, *160*, 725−733.

(38) Zhang, Y.; Li, S.; Ren, Y.; Yao, Q.; Tse, S. D. A New Diagnostic for Volume Fraction Measurement of Metal-Oxide Nanoparticles in Flames Using Phase-Selective Laser-Induced Breakdown Spectroscopy. *Proc. Combust. Inst.* **2015**, *35*, 3681−3688.

(39) Yang, X.; Yang, L.; Lin, S.; Zhou, R. New Insight into the Doping Effect of Pr2O3 on the Structure-Activity Relationship of Pd/CeO2-ZrO2 Catalysts by Raman and XRD Rietveld Analysis. *J. Phys. Chem. C* **2015**, *119*, 6065−6074.

(40) Ding, Y.; Wu, Q.; Lin, B.; Guo, Y.; Guo, Y.; Wang, Y.; Wang, L.; Zhan, W. Superior Catalytic Activity of a Pd Catalyst in Methane Combustion by Fine-Tuning the Phase of Ceria-Zirconia Support. *Appl. Catal., B* **2020**, *266*, 118631.

(41) He, Y.; Liang, X.; Chen, B. Surface Selective Growth of Ceria Nanocrystals by CO Absorption. *ChemComm* **2013**, *49*, 9000−9002.

(42) Li, J.; Liu, X.; Zhan, W.; Guo, Y.; Guo, Y.; Lu, G. Preparation of High Oxygen Storage Capacity and Thermally Stable Ceria-Zirconia Solid Solution. *Catal. Sci. Technol.* **2016**, *6*, 897−907.

(43) Bumajdad, A.; Nazeer, A. A.; Al Sagheer, F.; Nahar, S.; Zaki, M. I. Controlled Synthesis of ZrO2 Nanoparticles with Tailored Size, Morphology and Crystal Phases via Organic/Inorganic Hybrid Films. *Sci. Rep.* **2018**, *8*, 3695.

(44) Gnana Sundara Raj, B.; Asiri, A. M.; Wu, J. J.; Anandan, S. Synthesis of Mn3O4 Nanoparticles via Chemical Precipitation Approach for Supercapacitor Application. *J. Alloys Compd.* **2015**, *636*, 234−240.

(45) Johnson, C. S.; Dees, D. W.; Mansuetto, M. F.; Thackeray, M. M.; Vissers, D. R.; Argyriou, D.; Loong, C.-K.; Christensen, L. Structural and electrochemical studies of α-manganese dioxide (α-MnO2). *J. Power Sources* **1997**, *68*, 570−577.

(46) Shinde, P. A.; Lokhande, V. C.; Patil, A. M.; Yadav, A. A.; Lokhande, C. D. Hydrothermal Synthesis of Manganese Oxide Thin Films Using Different Oxidizing Agents for Supercapacitor Application. *Int. J. Eng. Res.* **2017**, *10*, 532−537.

(47) Wu, Y.; Cao, C.; Zhu, Y.; Li, J.; Wang, L. Cube-Shaped Hierarchical LiNi1/3Co1/3Mn1/3O2 with Enhanced Growth of Nanocrystal Planes as High-Performance Cathode Materials for Lithium-Ion Batteries. *J. Mater. Chem. A* **2015**, *3*, 15523−15528.

(48) Cabañas, A.; Darr, J. A.; Lester, E.; Poliakoff, M. Continuous Hydrothermal Synthesis of Inorganic Materials in a Near-Critical Water Flow Reactor; the One-Step Synthesis of Nano-Particulate Ce1-xZrxO2 (x=0-1) Solid Solutions. *J. Mater. Chem.* **2001**, *11*, 561−568.

(49) Sergent, N.; Lamonier, J. F.; Aboukaïs, A. Electron Paramagnetic Resonance in Combination with the Thermal Analysis, X-Ray Diffraction, and Raman Spectroscopy to Follow the Structural Properties of ZrxCe1-xO2 Solid Systems and Precursors. *Chem. Mater.* **2000**, *12*, 3830−3835.

(50) Wang, S.-P.; Zhang, T.-Y.; Su, Y.; Wang, S.-R.; Zhang, S.-M.; Zhu, B.-L.; Wu, S.-H. An Investigation of Catalytic Activity for CO Oxidation of CuO/CexZr1-xO2 Catalysts. *Catal. Lett.* **2008**, *121*, 70−76.

(51) Reddy, B. M.; Khan, A.; Lakshmanan, P.; Aouine, M.; Loridant, S.; Volta, J.-C. Structural Characterization of Nanosized CeO2−SiO2, CeO2−TiO2, and CeO2−ZrO2 Catalysts by XRD, Raman, and HREM Techniques. *J. Phys. Chem. B* **2005**, *109*, 3355−3363.

(52) Iqbal, Z.; Christoe, C. W. Raman Scattering Study of Phase Transition in Ammonium Sulfate. *Ferroelectrics* **1976**, *12*, 177−179.

(53) Wu, Z.; Li, M.; Howe, J.; Meyer, H. M.; Overbury, S. H. Probing Defect Sites on CeO_2 Nanocrystals with Well-Defined Surface Planes by Raman Spectroscopy and O_2 Adsorption. *Langmuir* **2010**, *26*, 16595−16606.

(54) Taniguchi, T.; Watanabe, T.; Sugiyama, N.; Subramani, A. K.; Wagata, H.; Matsushita, N.; Yoshimura, M. Identifying Defects in Ceria-Based Nanocrystals by UV Resonance Raman Spectroscopy. *J. Phys. Chem. C* **2009**, *113*, 19789−19793.

(55) Li, L.; Chen, F.; Lu, J. Q.; Luo, M. F. Study of Defect Sites in $Ce_{1-x}M_xO_{2-\delta}$ (x = 0.2) Solid Solutions Using Raman Spectroscopy. *J. Phys. Chem. A* **2011**, *115*, 7972−7977.

(56) Liu, G.; Yue, R.; Jia, Y.; Ni, Y.; Yang, J.; Liu, H.; Wang, Z.; Wu, X.; Chen, Y. Catalytic Oxidation of Benzene over Ce-Mn Oxides Synthesized by Flame Spray Pyrolysis. *Particuology* **2013**, *11*, 454−459.

(57) Wang, L.; Li, Y.; Han, Z.; Chen, L.; Qian, B.; Jiang, X.; Pinto, J.; Yang, G. Composite Structure and Properties of Mn_3O_4/Graphene Oxide and Mn_3O_4/Graphene. *J. Mater. Chem. A* **2013**, *1*, 8385−8397.

(58) Shah, H. U.; Wang, F.; Toufiq, A. M.; Ali, S.; Khan, Z. U. H.; Li, Y.; Hu, J.; He, K. Electrochemical Properties of Controlled Size Mn_3O_4 Nanoparticles for Supercapacitor Applications. *J. Nanosci. Nanotechnol.* **2018**, *18*, 719−724.

(59) Julien, C. M.; Massot, M.; Poinsignon, C. Lattice vibrations of manganese oxides. *Spectrochim. Acta, Part A* **2004**, *60*, 689−700.

(60) Venkataswamy, P.; Jampaiah, D.; Lin, F.; Alxneit, I.; Reddy, B. M. Structural Properties of Alumina Supported Ce-Mn Solid Solutions and Their Markedly Enhanced Catalytic Activity for CO Oxidation. *Appl. Surf. Sci.* **2015**, *349*, 299−309.

(61) Liu, Y. F.; Yuan, G. H.; Jiang, Z. H.; Yao, Z. P. Solvothermal Synthesis of Mn_3O_4 Nanoparticle/Graphene Sheet Composites and Their Supercapacitive Properties. *J. Nanomater.* **2014**, *2014*, 190529.

(62) Li, L.; Seng, K. H.; Liu, H.; Nevirkovets, I. P.; Guo, Z. Synthesis of Mn_3O_4-Anchored Graphene Sheet Nanocomposites via a Facile, Fast Microwave Hydrothermal Method and Their Supercapacitive Behavior. *Electrochim. Acta* **2013**, *87*, 801−808.

(63) Omata, T.; Kishimoto, H.; Otsuka-Yao-Matsuo, S.; Ohtori, N.; Umesaki, N. Vibrational Spectroscopic and X-Ray Diffraction Studies of Cerium Zirconium Oxides with Ce/Zr Composition Ratio=1 Prepared by Reduction and Successive Oxidation of T′-$(Ce_{0.5}Zr_{0.5})O_2$ Phase. *J. Solid State Chem.* **1999**, *147*, 573−583.